



Article

Synthesis of Superparamagnetic Fe₃O₄ Nano-Adsorbent Using an Energy-Saving and Pollution-Reducing Strategy for the Removal of Xylenol Orange Dye in Water

Yaohui Xu ¹, Qin Wang ¹ and Zhao Ding ^{2,*}

¹ Laboratory for Functional Materials, School of Electronics and Materials Engineering, Leshan Normal University, Leshan 614000, China

² National Engineering Research Center for Magnesium Alloys, College of Materials Science and Engineering, Chongqing University, Chongqing 400044, China

* Correspondence: zhaoding@cqu.edu.cn

Abstract: The superparamagnetic Fe₃O₄ nanoparticles as an adsorbent with a size distribution of 4.8–6.4 nm were synthesized using a simple one-pot hydrothermal strategy at 200 °C for 24 h, where iron citrate and distilled were the sum total of raw materials. The as-synthesized Fe₃O₄ powders showed rapid and efficient adsorption for xylenol orange with a saturated adsorption amount of 42.5 mg/g according to Langmuir linear fitting, and the adsorption reaction between xylenol orange adsorbate and Fe₃O₄ adsorbent was mostly completed within 10 min. The Fe₃O₄ nanoparticles not only had superparamagnetism with a saturation magnetization value of 54.9 emu/g at 15 kOe but also possessed strong magnetic response, making them easy to separate easily from aqueous solution under the attraction of magnet. In this work, the Fe₃O₄ particles can be totally attracted toward the magnet within 15 s, leaving the suspension a clear solution.

Keywords: iron citrate; magnetic Fe₃O₄; superparamagnetism; hydrothermal; adsorption; dye



Citation: Xu, Y.; Wang, Q.; Ding, Z. Synthesis of Superparamagnetic Fe₃O₄ Nano-Adsorbent Using an Energy-Saving and Pollution-Reducing Strategy for the Removal of Xylenol Orange Dye in Water. *Energies* **2022**, *15*, 7378. <https://doi.org/10.3390/en15197378>

Academic Editor: Kyu-Jung Chae

Received: 26 August 2022

Accepted: 28 September 2022

Published: 8 October 2022

Publisher's Note: MDPI stays neutral with regard to jurisdictional claims in published maps and institutional affiliations.



Copyright: © 2022 by the authors. Licensee MDPI, Basel, Switzerland. This article is an open access article distributed under the terms and conditions of the Creative Commons Attribution (CC BY) license (<https://creativecommons.org/licenses/by/4.0/>).

1. Introduction

Energy development and environmental protection have always been the common concern of people because energy is the important material base for the life and development of human society, and the environment is the fundamental condition for human survival [1–4]. Water pollution caused by dyes is a serious disposal problem because most of the dyes in water are highly visible and undesirable. The dyes can severely interfere with the absorption and reflection of sunlight entering the water, which affects the replication and producing of dye-degrading bacteria; as a result, these dyes are not biodegradable in the water [5–9]. Therefore, removal of such colored dye contaminants from polluted aqueous media has become an impendent issue. To solve this problem, a number of available technologies for the removal of dyestuffs have been developed and implemented, such as physical [10,11], chemical [12,13], electrical [14,15], and biological [16,17] strategies. Among these technologies, the adsorption technology has been regarded as one of the most competitive methods for wastewater treatment in terms of its flexibility and simplicity of design, operational ease, and insensitivity to pollutants; moreover, no harmful substances are formed during the adsorption reaction [18–20].

Many adsorbent materials have been developed to remove dyes from aqueous solution, such as graphene oxide nanocomposites [21], activated carbon [22], ultrafiltration membrane [23], natural fiber [24,25], and magnetic nanocellulose [26]. Among all available candidates, the nanostructured Fe₃O₄ particles are attractive because of their superparamagnetism, which facilitates the targeting control and recyclable separation just using an applied magnetic field. This superparamagnetism of Fe₃O₄ particles is beneficial to the simple and rapid separation of Fe₃O₄ after adsorption of pollutants, which can not only save the cost,

but also shorten the operation cycle. In addition, the size effect of nanomaterials makes them easier to capture the pollutant due to enhanced surface activity [27,28]. So far, numerous methods have been reported to synthesize magnetic Fe₃O₄ nanoparticles. For example, Chen et al. [29] synthesized the superparamagnetic Fe₃O₄ nanofibers with hollow characteristic morphology based on a polymer-assisted thermochemical reduction process, and the diameter and wall thickness of these nanofibers were ranging from 100 to 200 nm and 15 to 25 nm, respectively. Yang et al. [30] synthesized the magnetite (Fe₃O₄) nanoparticles with different shapes and sizes by the thermal decomposition method. Liu et al. [31] also synthesized Fe₃O₄ nanoparticles with a diameter of ~500 nm by a hydrothermal method using FeCl₃·6H₂O, ethylene glycol and CH₃COONa as the main raw materials. Moreover, Eskandari et al. [32] synthesized the Fe₃O₄ nanoparticles (6 nm) based on a chemical co-precipitation method with an alternating magnetic field and ultrasonic-assisted. Although these methods could synthesize the nanostructured Fe₃O₄ particles with superparamagnetism, but the synthesis process is still not the easiest, as well as the used raw materials. It is still challenging to further simplify the operation process to reduce costs and energy consumption.

Xylenol orange (XO) is a common synthetic dye, also usually used as potentiometric reagent and complexometric indicator for the determination of metal ions in the science laboratory. Therefore, the XO effluents from manufacturing industries and laboratories will further attract heavy metal ions, finally leading to various ailments to the living body. To date, only a few studies had reported on the removal of XO from the aqueous solution. Hyperbranched polyethyleneimine based gels [33] and polyvinyl alcohol/cellulose nanocrystals hydrogels [34] were developed as absorbent materials for the removal of XO from the aqueous solution. However, the process of collecting these used sorbents from water was cumbersome after the adsorption reaction. For that, in this work, a facile one-pot hydrothermal procedure was developed for the synthesis of superparamagnetic Fe₃O₄ nanoparticles, in which iron citrate and distilled were the sum total of raw materials. The main advantages of hydrothermal method are as follows. The cheap and readily available water served as the solvent during the hydrothermal method, which could synthesize the desired products under medium and low temperature conditions without subsequent high-heat treatment. The closed conditions of hydrothermal process could reduce the emission of toxic and harmful gases, effectively reducing environmental pollution, in line with the requirements of energy-saving and emission reduction. Moreover, the as-synthesized superparamagnetic Fe₃O₄ nanoparticles could serve as an adsorbent for the removal of XO, as a comparison, the adsorptions of other dyes, Basic Orange 2 (BO2) and Acid Orange 7 (AO7) were also investigated.

2. Experimental

2.1. Materials

Iron citrate (AR) was obtained from Shanghai Yien Chemical Technology Co., Ltd., Xylenol Orange (XO, 98%) dye was obtained from Shanghai Bide Medical Technology Co., Ltd., Basic Orange 2 (BO2, AR) dye was obtained from Shanghai Maclin Biochemical Technology Co., Ltd., Acid Orange 7 (AO7, >97.0%) was obtained from Tokyo Chemical Industry Co., Ltd., and ethanol (≥99.7%) was purchased from Chengdu Kelong Chemical Co., Ltd. The general characteristics of XO, BO2, and AO7 dyes, including Cas number, chemical number, and maximum absorption wavelength are (λ_{\max}), are shown in Table 1. These reagents were used as received without further purification.

2.2. Synthesis of Fe₃O₄

Superparamagnetic Fe₃O₄ nanoparticles were synthesized by a sample one-step hydrothermal procedure based on our previous report [35]. Iron citrate (4.0 mmol) and distilled water (30 mL) was directly added into a 50 mL Teflon-lined stainless-steel autoclave, and maintained for 24 h at 200 °C. After cooling to room temperature, the resulting precipitate was separated with the help of a magnet, and washed with distilled water and ethanol. Finally, the Fe₃O₄ powders were obtained under vacuum at 60 °C for 24 h.

2.3. Characterization

The crystallographic phase of Fe₃O₄ sample was characterized by X-ray diffraction (XRD, DX-2700). The morphology and size of Fe₃O₄ particles were evaluated by transmission electron microscopy (TEM, JEM-2100F). The magnetic property of Fe₃O₄ powders was obtained by physical performance measurement system (PPMS 9).

2.4. Evaluation of Adsorption Capacity

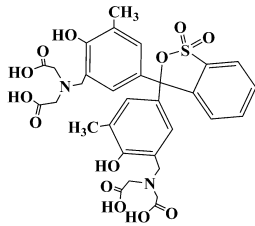
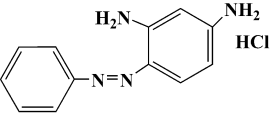
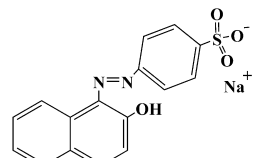
The adsorption capacities of Fe₃O₄ powders were evaluated by the removal of XO, BO2, and AO7 dyes from simulated wastewater at room temperature without pH preadjustment. Briefly, 0.1 g Fe₃O₄ powder was dispersed into 100 mL dye solution with different concentrations, and the mixture was stirred at a constant speed of 200 rpm. Then, a small amount of suspension was withdrawn at regular intervals and separated by an applied magnetic field, and the absorbance of supernatant was measured at the maximum absorption wavelength of the dye using an ultraviolet-visible spectrophotometer (U-3900). The adsorption efficiencies (η_t , %) and adsorption amount (q , mg/g) for dyes were calculated using Equations (1) and (2), respectively:

$$\eta_t = \frac{C_0 - C_t}{C_0} \times 100 \% \quad (1)$$

$$q = \frac{(C_0 - C_e)V}{m} \quad (2)$$

where C_0 (mg/L) is the initial concentration of dyes, C_t (mg/L) is the concentration of dyes at time t ($t = 0-60$ min), m (g) is the mass of Fe₃O₄ powders, and V (L) is the volume of dyes aqueous solution.

Table 1. General characteristics of AO7 dye.

Generic Name	Abbreviation	Cas Number	Chemical Structure	λ_{\max} (nm)
Xylenol orange	XO	1611-35-4		435
Basic orange 2	BO2	532-82-1		452
Acid orange 7	AO7	633-96-5		484

3. Results and Discussion

Figure 1a shows the XRD pattern of the sample. All broad peaks had a good match with the standard Fe₃O₄ pattern (JCPDS No. 65-3107), suggesting that the as-synthesized Fe₃O₄ particles had a good crystallinity with small grain size. The mean grain size of Fe₃O₄ was about 6.6 nm, as calculated by the Scherrer formula. Figure 1b shows the high-resolution XPS spectra of Fe 2p and O 1s of the as-synthesized Fe₃O₄ particles. For the Fe2p core-level XPS spectra, two distinct peaks with binding energies of 724.1 and 710.5 eV

appeared, which were assigned to the characteristic doublets of Fe 2p_{1/2} and Fe 2p_{3/2} from iron oxide. For the O 1s core-level XPS spectra in the inset of Figure 1b, the O 1s centered at binding energy of 529.8 eV belonged to O^{2−} species, and these data are consistent with the reported literature [36]. The above XRD and XPS results confirmed the formation of Fe₃O₄ phase in the hydrothermal system. TEM was employed to characterize the morphology and size of Fe₃O₄ particles. As observed in Figure 1c, the morphology of particles was an equiaxed shape. Moreover, these size values of Fe₃O₄ particles were demonstrated by a statistical analysis, the size distribution histograms were showed in Figure 1d, and most of the Fe₃O₄ particles were mainly concentrated in 4.8–6.4 nm.

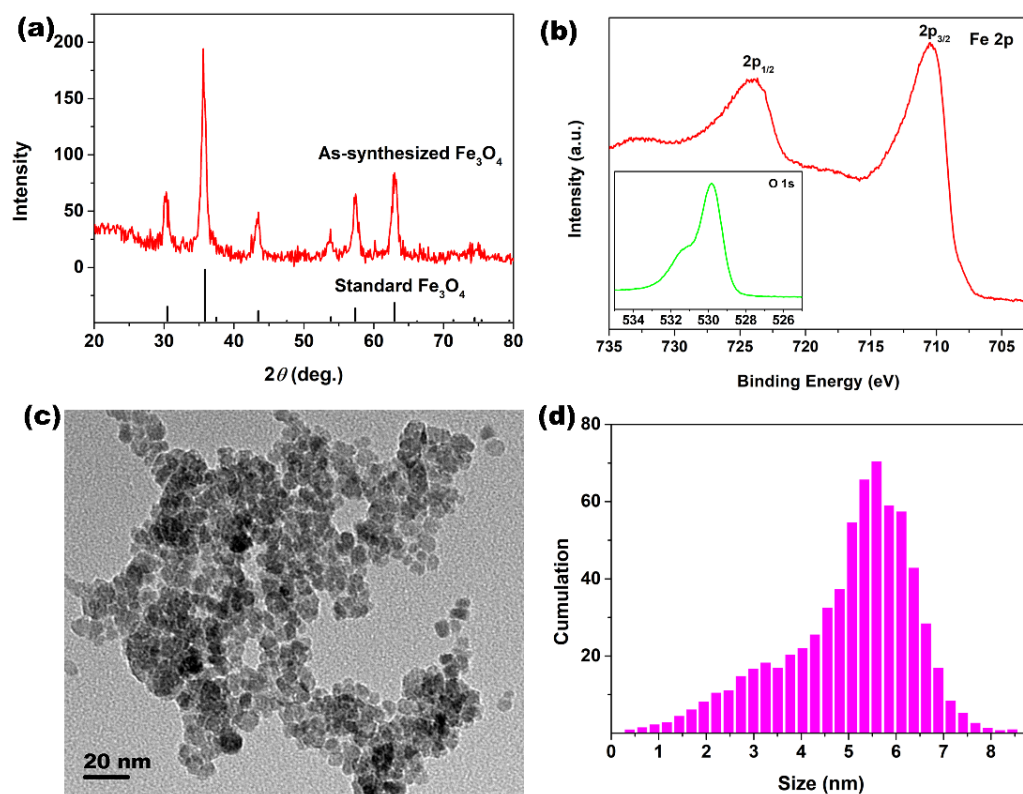


Figure 1. (a) XRD pattern of Fe₃O₄ powders; (b) high-resolution XPS spectra of Fe 2p (the inset is the high-resolution XPS spectra of O 1s); (c) TEM image; and (d) size distribution histogram of Fe₃O₄ particles.

The room-temperature magnetization hysteresis loop of the as-synthesized Fe₃O₄ was measured by a physical performance measurement system. Figure 2a shows the magnetic hysteresis curve of Fe₃O₄ powders. From Figure 2a, it could be found that the saturation magnetization value of Fe₃O₄ nanoparticles was 54.9 emu/g. Moreover, the Fe₃O₄ nanoparticles were essentially superparamagnetic with negligible hysteresis, as observed by the enlarged partial curve of the surrounding origin in Figure 2a. In practical application, it is critical for practical applications that the magnetic materials should exhibit prompt responsiveness to an applied magnetic field without retaining any magnetism once the applied magnetic field was removed [37]. The magnetic manipulation of such superparamagnetic Fe₃O₄ was performed in water upon the application of a NdFeB permanent magnet near the glass bottle. As observed in Figure 2c, the Fe₃O₄ particles can be totally attracted toward the magnet within 15 s, leaving the suspension a clear solution. Moreover, the congregated Fe₃O₄ particles can be easily and quickly re-dispersed again by shaking after the removal of magnet. Hence, this superparamagnetic Fe₃O₄ powders have the potential to be easily recovered after liquid phase adsorption reaction, which could greatly facilitate the practical running of an industrial pollutant cleanup.

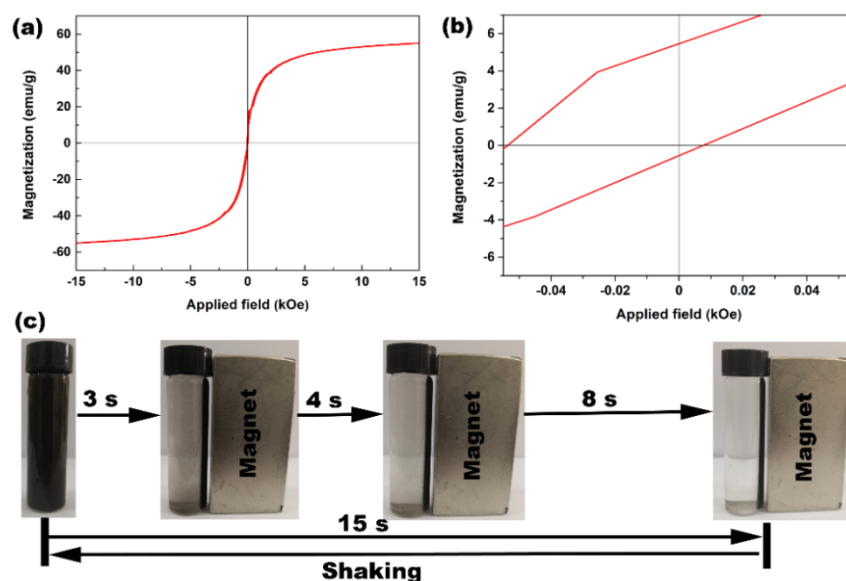


Figure 2. (a) Magnetic hysteresis curve of Fe_3O_4 powders and (b) enlarged partial curve of the surrounding origin in (a); (c) pictures for the progressive separation of Fe_3O_4 particles from aqueous medium upon the application of a NdFeB permanent magnet ($[\text{Fe}_3\text{O}_4] = 25.0 \text{ g/L}$; $V = 8.0 \text{ mL}$; Distilled water; Glass bottle: $d = 1.5 \text{ cm}$ and $h = 6.2 \text{ cm}$).

Figure 3 shows that the time-dependent adsorption efficiencies of superparamagnetic Fe_3O_4 nanoparticles for XO, BO2, and AO7 dyes. It was observed that Fe_3O_4 nanoparticles had larger adsorption affinity for XO dye, whereas the adsorption of AO7 dye can be ignored. The adsorption efficiencies achieved within 60 min of reaction was 98.5, 15.9, and 5.5% for XO, BO2, and AO7 dyes, respectively. Furthermore, it could be clearly observed that the adsorption of XO dye was rapid at the early stages of the process. In fact, the adsorption reaction was mostly completed within 10 min, and the removal rate was up to 93.6%. No significant changes were observed from 20 to 60 min, indicating that the adsorption-desorption equilibrium between the dye adsorbate and Fe_3O_4 adsorbent was reached within the first 10 min of adsorption reactions. Compared with the adsorption reaction of XO dye, those of BO2 and AO7 dyes reached the adsorption-desorption equilibrium within 30 min, and the removal rates were only 23.0 and 6.2%.

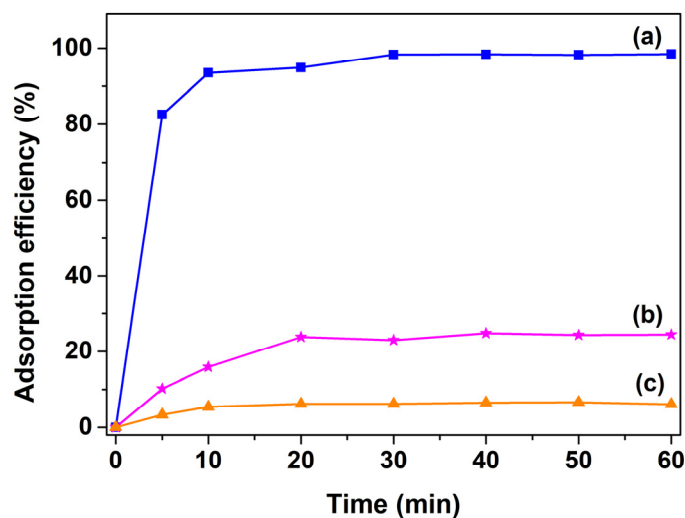


Figure 3. Time-dependence of adsorption profiles of (a) XO; (b) BO2; and (c) AO7 dyes with the presence of superparamagnetic Fe_3O_4 powders. ($[\text{Fe}_3\text{O}_4] = 1.0 \text{ g/L}$; $[\text{dye}] = 10 \text{ mg/L}$; Room temperature; without pH preadjustment).

The saturated adsorption amounts (q_m) of XO, BO2, and AO7 dyes were obtained according to the Langmuir isotherm model, and the Langmuir linear fittings based on the adsorption data of these dyes onto the superparamagnetic Fe_3O_4 nanoparticles were showed in Figure 4a–c, while the relevant parameters of Langmuir fittings calculated were listed in Table 2. By comparing with the associated correlation coefficients (R^2), it could be found that the Langmuir isotherm model was most suitable for modeling the adsorption of XO dye ($R^2 = 0.9991$) than that of BO2 ($R^2 = 0.9546$) and AO7 ($R^2 = 0.7904$) dyes, and the value of q_m is 42.5 mg/g for XO dye according to the Langmuir linear fitting. Table 3 shows the q_m values of XO dye adsorbed on other adsorbents from the recent literature [33,38–42]. Despite the adsorption capacity of superparamagnetic Fe_3O_4 nanoparticles synthesized in this work being moderate among these reported adsorbents by comparing the q_m of various adsorbents, the Fe_3O_4 adsorbent still had obvious advantages in energy consumption and cost, which are due to the advantages of synthetic process and the superparamagnetism of Fe_3O_4 nanoparticles synthesized in this work. The equipment used in the hydrothermal process was simple and economical, and the Fe_3O_4 phase could be obtained in a simple one-pot hydrothermal process. In addition, the as-synthesized Fe_3O_4 nanoparticles in this work had excellent magnetic sensitivity, which made them easy to separate from liquid medium under the attraction of a magnet.

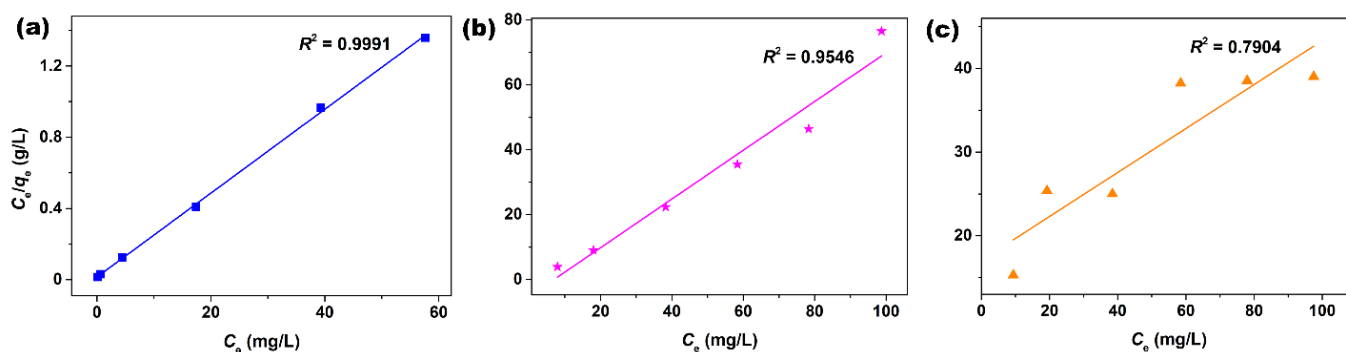


Figure 4. Langmuir linear fittings of (a) XO, (b) BO2, and (c) AO7 dyes adsorbed onto the superparamagnetic Fe_3O_4 nanoparticles.

Table 2. Relevant parameters of Langmuir fittings for XO, BO2, and AO7 dyes adsorbed onto the superparamagnetic Fe_3O_4 powders.

Langmuir Parameters	Langmuir Isotherm Model: $\frac{C_e}{q_e} = \frac{1}{q_m} C_e + \frac{1}{K_L q_m}$		
	XO Dye	BO2 Dye	AO7 Dye
q_m (mg/g)	42.5	1.3	3.8
R^2	0.9991	0.9546	0.7904

Table 3. Recent literature on adsorbent development for the removal of XO dye.

Authors	Adsorbent Name	Synthetic Method	q_m (mg/g)
Ishaq [38]	Coal ash	Heated at 750 °C	0.74
Bai [39]	Porous amino-cellulose membrane	TEMPO oxidation and ethylenediamine grafting	15
Pang [40]	Expansion graphite	Chemical oxidation intercalation of potassium permanganate and vitriol	18.15
Garrudo-Guirado [41]	Vitreous tuff mineral (VT)	Milled and sieved to 60 mesh	45.17
Wang [42]	Bi-porous chitosan monoliths	Unidirectional freeze-drying method under vacuum less than 20 Pa for 48 h	153.8
Zhu [33]	Hyperbranched polyethyleneimine (HPEI) based gel	Cross-linking reaction between HPEI and N,N' -methylene-bis-acrylamide	3312.06
Xu in this work	Fe_3O_4 nanoparticles	One-pot hydrothermal process at 200 °C for 24 h	42.5

The sorption kinetics of XO, BO2, and AO7 dyes onto Fe₃O₄ nanoparticles were tested using a pseudo-first-order kinetic model by plotting $\log(q_e - q_t)$ versus t (Figure 5a,c,e), as well as pseudo-second-order kinetic model by plotting t/q_t versus t (Figure 5b,d,f). As observed in Figure 5, the adsorption of XO, BO2, and AO7 dyes using a pseudo-second-order model (Figure 5b,d,f) exhibited a better linear fit than those using a pseudo-first-order model (Figure 5a,c,e). Moreover, the relevant kinetic parameters, such as the equilibrium adsorption amount ($q_{e1,cal}$, $q_{e2,cal}$), rate constant (k_1 and k_2), and correlation coefficient (R^2), could be obtained by fitting with these two models, and the results were listed in Table 4. As observed in Table 4, all pseudo-second-order equations showed higher correlation coefficients ($R^2 > 0.98$) than their respective pseudo-first-order equations ($R^2 < 0.74$), and the adsorption amounts at equilibrium ($q_{e,cal}$) were much closer to the respective experimental one ($q_{e,exp}$). Therefore, the pseudo-second order model is more suitable to describe the adsorption kinetics of XO, BO2, and AO7 dyes onto Fe₃O₄ nanoparticles, indicating that the chemisorption is the rate controlling step during the attachment process.

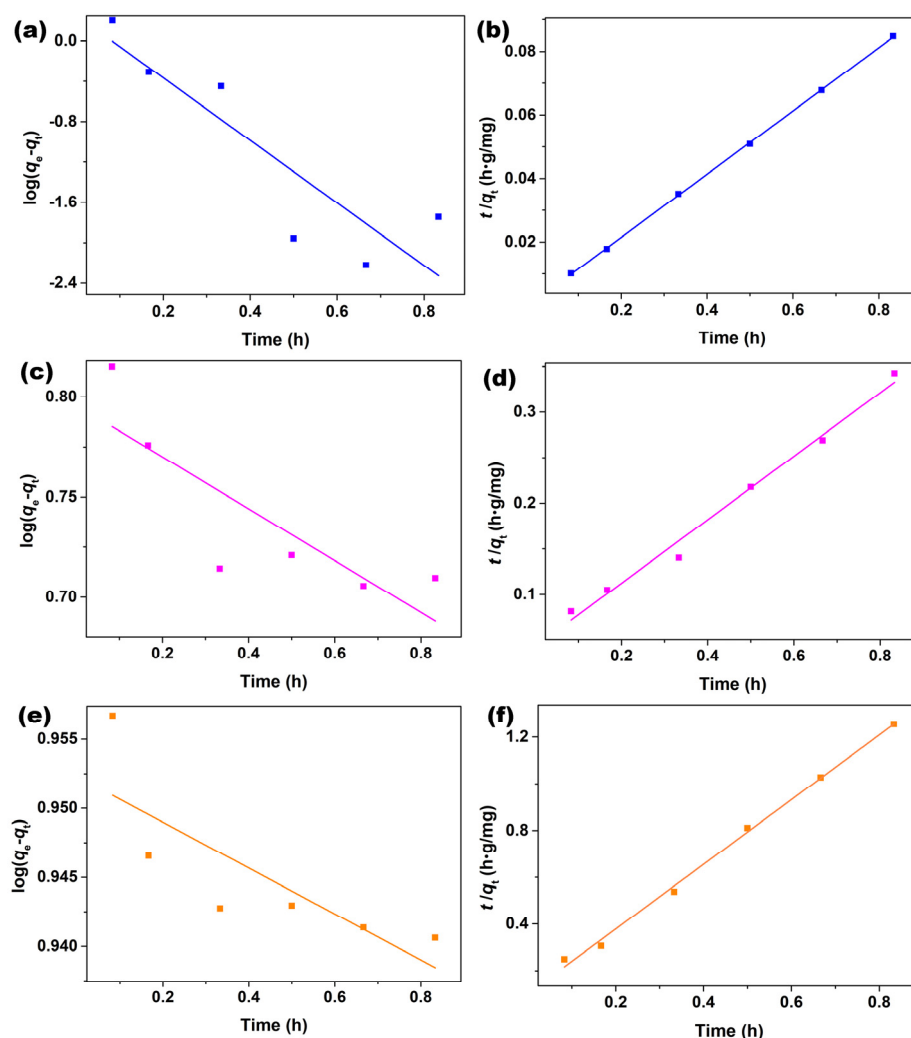


Figure 5. Fittings by a pseudo-first-order model for the adsorption of (a) XO, (c) BO2, and (e) AO7 dyes, pseudo-second-order model for the adsorption of (b) XO, (d) BO2, and (f) AO7 dyes onto Fe₃O₄ nanoparticles. ($[Fe_3O_4] = 1.0$ g/L; $[dye] = 10$ mg/L; Room temperature; without pH preadjustment).

Table 4. Kinetic parameters for the adsorption of XO, BO2, and AO7 dyes onto Fe₃O₄ nanoparticles at room temperature.

Dye	$q_{e,exp}$ (mg/g)	Pseudo-First-Order Kinetic Model			Pseudo-Second-Order Kinetic Model		
		$q_{e1,cal}$ (mg/g)	k_1 (1/h)	R^2	$q_{e2,cal}$ (mg/g)	k_1 (g/mg·h)	R^2
XO	9.847	1.7906	7.1318	0.7328	10.0452	6.4352	0.9998
BO2	2.444	6.2516	0.2983	0.6316	2.8740	2.8272	0.9859
AO7	0.614	8.9600	0.0383	0.5564	0.7223	18.9232	0.9959

4. Conclusions

In summary, Fe₃O₄ nanoparticles with a main size distribution of 4.8–6.4 nm have been successfully synthesized via a simple one-pot hydrothermal strategy at 200 °C for 24 h, in which iron citrate and distilled were the sum total of raw materials. The as-synthesized Fe₃O₄ nanoparticles exhibited apparent superparamagnetism, and the saturation magnetization value was 54.9 emu/g. Moreover, Fe₃O₄ nanoparticles possessed sensitive magnetic responsiveness, which can be totally attracted toward the magnet within 15 s from suspension, and quickly re-dispersed again by shaking after the removal of magnet. Such superparamagnetic Fe₃O₄ nanoparticles exhibited the effective adsorption affinity for XO dye, and the adsorption reactions were mostly completed within 10 min. The Langmuir isotherm model is most suitable for modeling the adsorption of XO dye ($R^2 = 0.9991$) compared to those of BO2 and AO7 dyes, and the value of the saturated adsorption amount is 42.5 mg/g for XO dye according to Langmuir linear fitting. This superparamagnetic Fe₃O₄ nanoparticles had the potential to be easily recovered after liquid phase adsorption reaction, which could greatly facilitate the practical running of an industrial pollutant cleanup.

Author Contributions: Conceptualization, methodology, writing—original draft preparation, writing—review and editing, resources, Y.X.; validation, formal analysis, investigation, data curation, Q.W.; resources, visualization, project administration, funding acquisition, Z.D. All authors have read and agreed to the published version of the manuscript.

Funding: This research was funded by [Leshan Normal University Research Program, China] grant number [2021SSDJS012], [Science and Technology Bureau of Leshan city of China] grant number [22ZDYJ0093], and [Fundamental Research Funds for the Central Universities] grant number [2022CDJXY-010].

Conflicts of Interest: The authors declare no conflict of interest.

References

- Ding, Z.; Yang, W.; Huo, K.; Shaw, L. Thermodynamics and Kinetics Tuning of LiBH₄ for Hydrogen Storage. *Prog. Chem.* **2021**, *33*, 1586–1597. [CrossRef]
- Turky, A.O.; Rashad, M.M.; Hassan, A.M.; Elnaggar, E.M.; Bechelany, M. Optical, electrical and magnetic properties of lanthanum strontium manganite La_{1-x}Sr_xMnO₃ synthesized through the citrate combustion method. *Phys. Chem. Chem. Phys.* **2017**, *19*, 6878–6886. [CrossRef]
- Ding, Z.; Chen, Z.; Ma, T.; Lu, C.T.; Ma, W.; Shaw, L. Predicting the hydrogen release ability of LiBH₄-based mixtures by ensemble machine learning. *Energy Storage Mater.* **2020**, *27*, 466–477. [CrossRef]
- Turky, A.O.; Rashad, M.M.; Hassan, A.M.; Elnaggar, E.M.; Bechelany, M. Tailoring optical, magnetic and electric behavior of lanthanum strontium manganite La_{1-x}Sr_xMnO₃ (LSM) nanopowders prepared via a co-precipitation method with different Sr²⁺ ion contents. *RSC Adv.* **2016**, *6*, 17980–17986. [CrossRef]
- De Oca, R.M.G.F.-M.; Ramos-Leal, J.A.; Solache-Rios, M.J.; Martínez-Miranda, V.; Fuentes-Rivas, R.M. Modification of the Relative Abundance of Constituents Dissolved in Drinking Water Caused by Organic Pollution: A Case of the Toluca Valley, Mexico. *Water Air Soil Poll.* **2019**, *230*, 171. [CrossRef]
- Ding, Z.; Li, H.; Shaw, L. New Insights into the Solid-State Hydrogen Storage of Nanostructured LiBH₄-MgH₂ System. *Chem. Eng. J.* **2019**, *385*, 123856. [CrossRef]
- Yaseen, D.A.; Scholz, M. Comparison of Experimental Ponds for the Treatment of Dye Wastewater under Controlled and Semi-natural Conditions. *Environ. Sci. Pollut. Res.* **2017**, *24*, 16031–16040. [CrossRef]

8. Ding, Z.; Li, S.; Zhou, Y.; Chen, Z.; Zhang, F.; Wu, P.; Ma, W. LiBH_4 for Hydrogen Storage: New Perspectives. *Nano Mater. Sci.* **2020**, *2*, 109–119. [[CrossRef](#)]
9. Hashmi, S.S.; Shah, M.; Muhammad, W.; Ahmad, A.; Ullah, M.A.; Nadeem, M.; Abbasi, B.H. Potentials of Phyto-fabricated Nanoparticles as Ecofriendly Agents for Photocatalytic Degradation of Toxic Dyes and Waste Water Treatment, Risk Assessment and Probable Mechanism. *J. Indian Chem. Soc.* **2021**, *98*, 100019. [[CrossRef](#)]
10. Wang, J.; Zhang, Q.; Liu, J.; Ji, X.; Ma, J.; Tian, G. Preparation and Excellent Adsorption of water Pollution Dyes over Magnetic $\text{Fe}_3\text{O}_4/\text{C}$ Nanoparticles with Hollow Grape Cluster Morphology. *J. Nanopart. Res.* **2020**, *22*, 196. [[CrossRef](#)]
11. Huong, D.T.M.; Chai, W.S.; Show, P.L.; Lin, Y.L.; Chiu, C.Y.; Tsai, S.L.; Chang, Y.K. Removal of Cationic Dye Waste by Nanofiber Membrane Immobilized with Waste Proteins. *Int. J. Biol. Macromol.* **2020**, *164*, 3873–3884. [[CrossRef](#)] [[PubMed](#)]
12. Zheng, X.; Zheng, H.; Zhao, R.; Xiong, Z.; Wang, Y.; Sun, Y.; Ding, W. Sulfonic Acid-modified Polyacrylamide Magnetic Composite with Wide pH Applicability for Efficient Removal of Cationic Dyes. *J. Mol. Liq.* **2020**, *319*, 114161. [[CrossRef](#)]
13. Qi, J.; Wen, J.; Wang, Q.; Jin, X.; Zhou, X. Preparation and Photocatalytic Properties of Hexagonal and Orthogonal CuS Micro-nanoparticles by an Oil-water Interface Method. *Mater. Chem. Phys.* **2020**, *255*, 123629. [[CrossRef](#)]
14. Fan, T.; Deng, W.; Feng, X.; Pan, F.; Li, Y. An Integrated Electrocoagulation-Electrocatalysis Water Treatment Process using Stainless Steel Cathodes Coated with Ultrathin TiO_2 Nanofilms. *Chemosphere* **2020**, *254*, 126776. [[CrossRef](#)] [[PubMed](#)]
15. Kiwaan, H.A.; Mohamed, F.S.; El-Ghamaz, N.A.; Beshry, N.M.; El-Bindary, A.A. Experimental and Electrical Studies of Na-X zeolite for the Adsorption of Different Dyes. *J. Mol. Liq.* **2021**, *332*, 115877. [[CrossRef](#)]
16. Feizpoor, S.; Habibi-Yangjeh, A.; Chand, H.; Krishnan, V. Integration of Bi_5O_7 with TiO_2 : Binary Photocatalysts with Boosted Visible-light Photocatalysis in Removal of Organic Contaminants. *J. Photochem. Photobiol. A* **2021**, *410*, 113190. [[CrossRef](#)]
17. Sosa-Martínez, J.D.; Balagurusamy, N.; Montañez, J.; Peralta, R.A.; de Fátima Peralta-Muniz-Moreira, R.; Bracht, A.; Peralta, R.M.; Morales-Oyervides, L. Synthetic Dyes Biodegradation by Fungal Ligninolytic Enzymes: Process Optimization, Metabolites Evaluation and Toxicity Assessment. *J. Hazard. Mater.* **2020**, *400*, 123254. [[CrossRef](#)] [[PubMed](#)]
18. Xiong, X.L.; Shao, C.B. Removal of Xylenol Orange from Solutions by γ -Cyclodextrin-Grafted Carboxymethyl Cellulose. *Adv. Mater. Res.* **2011**, *204–210*, 1180–1183. [[CrossRef](#)]
19. Ding, Z.; Lu, Y.; Li, L.; Shaw, L. High Reversible Capacity Hydrogen Storage Through Nano- LiBH_4 + Nano- MgH_2 System. *Energy Storage Mater.* **2019**, *20*, 24–35. [[CrossRef](#)]
20. Ding, Z.; Wu, P.; Shaw, L. Solid-state Hydrogen Desorption of 2 MgH_2 + LiBH_4 Nano-mixture: A Kinetics Mechanism Study. *J. Alloys Compd.* **2019**, *806*, 350–360. [[CrossRef](#)]
21. Bayantong, A.R.B.; Shih, Y.-J.; Ong, D.C.; Abarca, R.R.M.; Dong, C.-D.; de Luna, M.D.G. Adsorptive Removal of Dye in Wastewater by Metal Ferrite-enabled Graphene Oxide Nanocomposites. *Chemosphere* **2021**, *274*, 129518. [[CrossRef](#)] [[PubMed](#)]
22. Ren, L.; Zhao, G.; Pan, L.; Chen, B.; Chen, Y.; Zhang, Q.; Xiao, X.; Xu, W. Efficient Removal of Dye from Wastewater without Selectivity Using Activated Carbon-Juncus Effusus Porous Fibril Composites. *ACS Appl. Mater. Interfaces* **2021**, *13*, 19176–19186. [[CrossRef](#)] [[PubMed](#)]
23. Ghadhban, M.Y.; Majdi, H.S.; Rashid, K.T.; Alsahy, Q.F.; Lakshmi, D.S.; Salih, I.K.; Figoli, A. Removal of Dye from a Leather Tanning Factory by Flat-Sheet Blend Ultrafiltration (UF) Membrane. *Membranes* **2020**, *10*, 47. [[CrossRef](#)] [[PubMed](#)]
24. Raja, Y.S.; Samsudin, M.F.R.; Sufian, S. Development of the Low-Cost and Green Hibiscus cannabinus Bioadsorbent for the Removal of Dye in Wastewater. *Arab. J. Sci. Eng.* **2020**, *46*, 6349–6358. [[CrossRef](#)]
25. Bayomie, O.S.; Kandeel, H.; Shoeib, T.; Yang, H.; Youssef, N.; El-Sayed, M.M.H. Novel Approach for Effective Removal of Methylene Blue Dye from Water using Fava Bean Peel Waste. *Sci. Rep.* **2020**, *10*, 7824. [[CrossRef](#)]
26. Amiralian, N.; Mustapic, M.; Hossain, M.S.A.; Wang, C.; Konarova, M.; Tang, J.; Na, J.; Khan, A.; Rowan, A. Magnetic nanocellulose: A Potential Material for Removal of Dye from Water. *J. Hazard. Mater.* **2020**, *394*, 122571. [[CrossRef](#)]
27. Turkey, A.O.; Mohamed Rashad, M.; Taha Kandil, A.E.-H.; Bechelany, M. Tuning the optical, electrical and magnetic properties of $\text{Ba}_{0.5}\text{Sr}_{0.5}\text{Ti}_x\text{M}_{1-x}\text{O}_3$ (BST) nanopowders. *Phys. Chem. Chem. Phys.* **2015**, *17*, 12553–12560. [[CrossRef](#)]
28. Turkey, A.O.; Rashad, M.M.; Bechelany, M. Tailoring optical and dielectric properties of $\text{Ba}_{0.5}\text{Sr}_{0.5}\text{TiO}_3$ powders synthesized using citrate precursor route. *Mater. Des.* **2016**, *90*, 54–59. [[CrossRef](#)]
29. Chen, S.; Chi, M.; Zhu, Y.; Gao, M.; Wang, C.; Lu, X. A Facile Synthesis of Superparamagnetic Fe_3O_4 Nanofibers with Superior Peroxidase-like Catalytic Activity for Sensitive Colorimetric Detection of L-cysteine. *Appl. Surf. Sci.* **2018**, *440*, 237–244. [[CrossRef](#)]
30. Yang, J.; Kou, Q.; Liu, Y.; Wang, D.; Lu, Z.; Chen, L.; Zhang, Y.Y.; Wang, Y.; Zhang, Y.J.; Han, D.; et al. Effects of Amount of Benzyl Ether and Reaction Time on the Shape and Magnetic Properties of Fe_3O_4 Nanocrystals. *Powder Technol.* **2017**, *319*, 53–59. [[CrossRef](#)]
31. Liu, X.; Huang, Y.; Ding, L.; Zhao, X.; Liu, P.; Li, T. Synthesis of Covalently Bonded Reduced Graphene Oxide- Fe_3O_4 Nanocomposites for Efficient Electromagnetic Wave Absorption. *J. Mater. Sci. Technol.* **2020**, *72*, 93–103. [[CrossRef](#)]
32. Eskandari, M.J.; Hasanzadeh, I. Size-controlled Synthesis of Fe_3O_4 Magnetic Nanoparticles via an Alternating Magnetic Field and Ultrasonic-assisted Chemical Co-precipitation. *Mater. Sci. Eng. B Adv.* **2021**, *266*, 115050. [[CrossRef](#)]
33. Zhu, C.; Xia, Y.; Zai, Y.; Dai, Y.; Liu, X.; Bian, J.; Liu, J.; Li, G. Adsorption and Desorption Behaviors of HPEI and Thermoresponsive HPEI based Gels on Anionic and Cationic Dyes. *Chem. Eng. J.* **2019**, *369*, 863–873. [[CrossRef](#)]
34. Bai, H.; Li, Z.; Zhang, S.; Wang, W.; Dong, W. Interpenetrating Polymer Networks in Polyvinyl Alcohol/cellulose Nanocrystals Hydrogels to Develop Absorbent Materials. *Carbohydr. Polym.* **2018**, *200*, 468–476. [[CrossRef](#)]

35. Xu, Y.; Wang, T.; Sun, D.; Li, R. Facile Synthesis of Superparamagnetic Fe₃O₄ Nanoparticles Just using Ferric Citrate and Water. *Integr. Ferroelectr.* **2016**, *176*, 179–183. [[CrossRef](#)]
36. Zhu, M.; Diao, G. Synthesis of Porous Fe₃O₄ Nanospheres and Its Application for the Catalytic Degradation of Xylenol Orange. *J. Phys. Chem. C* **2011**, *115*, 313–318. [[CrossRef](#)]
37. Lu, A.H.; Salabas, E.L.; Schüth, F. Magnetic Nanoparticles: Synthesis, Protection, Functionalization, and Application. *Angew. Chem. Int. Ed.* **2007**, *46*, 1222–1244. [[CrossRef](#)] [[PubMed](#)]
38. Ishaq, M.; Saeed, K.; Ahmad, I.; Sultan, S.; Akhtar, S. Coal ash as a low cost adsorbent for the removal of xylenol orange from aqueous solution. *Iran. J. Chem. Chem. Eng.* **2014**, *33*, 53–58. Available online: <https://www.researchgate.net/publication/293158575> (accessed on 1 March 2014).
39. Bai, Q.; Wang, W.; Liang, T.; Bai, H.Y.; Liu, X.Y. Preparation of porous amino-cellulose membrane and their adsorption performance of xylenol orange. *J. Cellul. Sci. Technol.* **2017**, *25*, 30–37. [[CrossRef](#)]
40. Pang, X.; Yang, C.; Ren, S. Adsorption capacity of expansion graphite for xylenol orange. *J. Mater. Sci. Chem. Eng.* **2013**, *1*, 1–5. [[CrossRef](#)]
41. Garrudo-Guirado, M.I.; Blanco-Flores, A.; Toledo-Jaldin, H.P.; Sanchez-Mendieta, V.; Vilchis-Nestor, A.R. Reuse of sustainable materials for xylenol orange dye and copper (II) ion ammoniacal removal. *J. Environ. Manag.* **2018**, *206*, 920–928. [[CrossRef](#)]
42. Wang, X.; Kong, W.; Xie, W.; Li, L.; Liu, Y.; Wu, X.; Gao, J. Bi-porous bioinspired chitosan foams with layered structure and their adsorption for xylenol orange. *Chem. Eng. J.* **2012**, *197*, 509–516. [[CrossRef](#)]